Role of Fault Geometry in Generating Backward-migrating P-wave Radiation During the 2025 Mw 7.7 Myanmar Earthquake

K. Tarumi[1,*] and K. Yoshizawa[1]

[1] Department of Earth & Planetary Sciences, Faculty of Science, Hokkaido University, Sapporo 060-0810, Japan.

[*]Corresponding author: tarumi.kotaro.jp@gmail.com

This is a revised preprint submitted to EarthArXiv. The revised manuscripts have been resubmitted to *Journal of Seismology* Special Issue on the 28 March 2025 Myanmar earthquake, following peer review.

Role of Fault Geometry in Generating Backward-migrating P-wave Radiation During the 2025 Mw 7.7 Myanmar Earthquake

Kotaro Tarumi[1,2*] and Kazunori Yoshizawa[1]

[1]Department of Earth and Planetary Sciences, Faculty of Science, Hokkaido University, Sapporo, 0600810, Japan.
[2]Earthquake Research Institute, The University of Tokyo, Tokyo, 113-0032, Japan.

*Corresponding author(s). E-mail(s): tarumi.kotaro.jp@gmail.com;
Contributing authors: yoshizawa@sci.hokudai.ac.jp;

Abstract

The Mw 7.7 Myanmar earthquake of 28 March 2025 ruptured the Sagaing Fault system over ∼450 km and exhibited complex rupture behavior, including intermittent supershear propagation and backward-migrating high-frequency (HF) P-wave radiation. We image the rupture evolution using multi-frequency teleseismic P-wave back-projection (BP) (0.05–0.5, 0.1–1.0, and 0.3–2.0 Hz) and compare the results with near-fault strong-motion data recorded at Nay Pyi Taw (NPT). Our BP results reveal two key features: (1) two distinct episodes of backward-migrating HF radiation initiated at the Sagaing–Meiktila and Meiktila–NPT fault junctions, with apparent migration speeds of 6.0–6.5 km/s, and (2) a pronounced HF radiator concentrated on a short splay-fault branch adjacent to the NPT segment. These HF radiators are preferentially located near the edges of high slip-rate patches in a P-wave slip model. The near-field displacement record at NPT shows a negative pulse following the quasi-static offset, likely representing a stopping phase generated by abrupt rupture arrest. Our results suggest that spatial variations in fault geometry, including segment junctions and fault branching, played an important role in rupture deceleration and termination, generating backward-migrating stopping-phase radiation.

Keywords: Myanmar earthquake; Back projection; High-frequency radiation; Stopping phase; Supershear rupture; Fault geometry

Highlights

- Multi-frequency P-wave radiators reveal backward-migrating P-wave radiation at supershear speeds.
- These episodes initiate at major segment junctions and are marked by high-frequency P-waves.
- They reflect backward-migrating stopping-phase radiation linked to fault bends and branching.

1 Introduction

On March 28th, 2025, a Mw 7.7 earthquake occurred along the Sagaing Fault in Myanmar, exhibiting a predominantly vertical strike-slip mechanism (Figure 1; USGS, 2025; Ekström et al, 2012). The Sagaing Fault is a major right-lateral strike-slip fault that accommodates slip partitioning associated with oblique convergence between the Indian and Sunda plates and extends for ∼1200 km, making it one of the longest active strike-slip faults in Southeast Asia (e.g., Wang et al, 2014). The source region consists of four principal segments, Sagaing (SGN), Meiktila (MKT), Nay Pyi Taw (NPT), and Pyu, forming a geometrically segmented fault system (Figure 1; Wang et al (2014)). Notably, a short splay fault branches from the junction between the MKT and NPT segments.

Historically, Mw 6–7 earthquakes have occurred along the SGN, NPT, and Pyu segments (Figure 1; Wang et al, 2014; Hurukawa and Maung, 2011), whereas the Meiktila segment has been regarded as a seismic gap due to the absence of documented large events (Hurukawa and Maung, 2011). Contrary to this historical pattern, recent seismological and geodesic studies indicate that the 2025 Mw 7.7 earthquake ruptured this seismic gap and propagated southward over an exceptionally long distance of ∼300–500 km (e.g., Inoue et al, 2025a; Ye et al, 2025; Lindsey et al, 2025; Xu et al, 2025).

Most studies agree that the rupture predominantly propagated southward at supershear speeds, based on finite-fault inversions (e.g., Inoue et al, 2025a; USGS, 2025; Lindsey et al, 2025; Li et al, 2025) and teleseismic P-wave back-projection (BP) analyses (e.g., Yao et al, 2025; Vera et al, 2025). Comparisons between BP results and near-field strong-motion records at Nay Pyi Taw (GE.NPW; Figure 1) suggest rupture-front velocities exceeding 4.0 km/s (Vera et al, 2025; Ye et al, 2025). Dynamic rupture simulations further support southward supershear propagation (Li et al, 2025). In addition, Hirano et al (2025) suggested intermittent transitions between sub- and

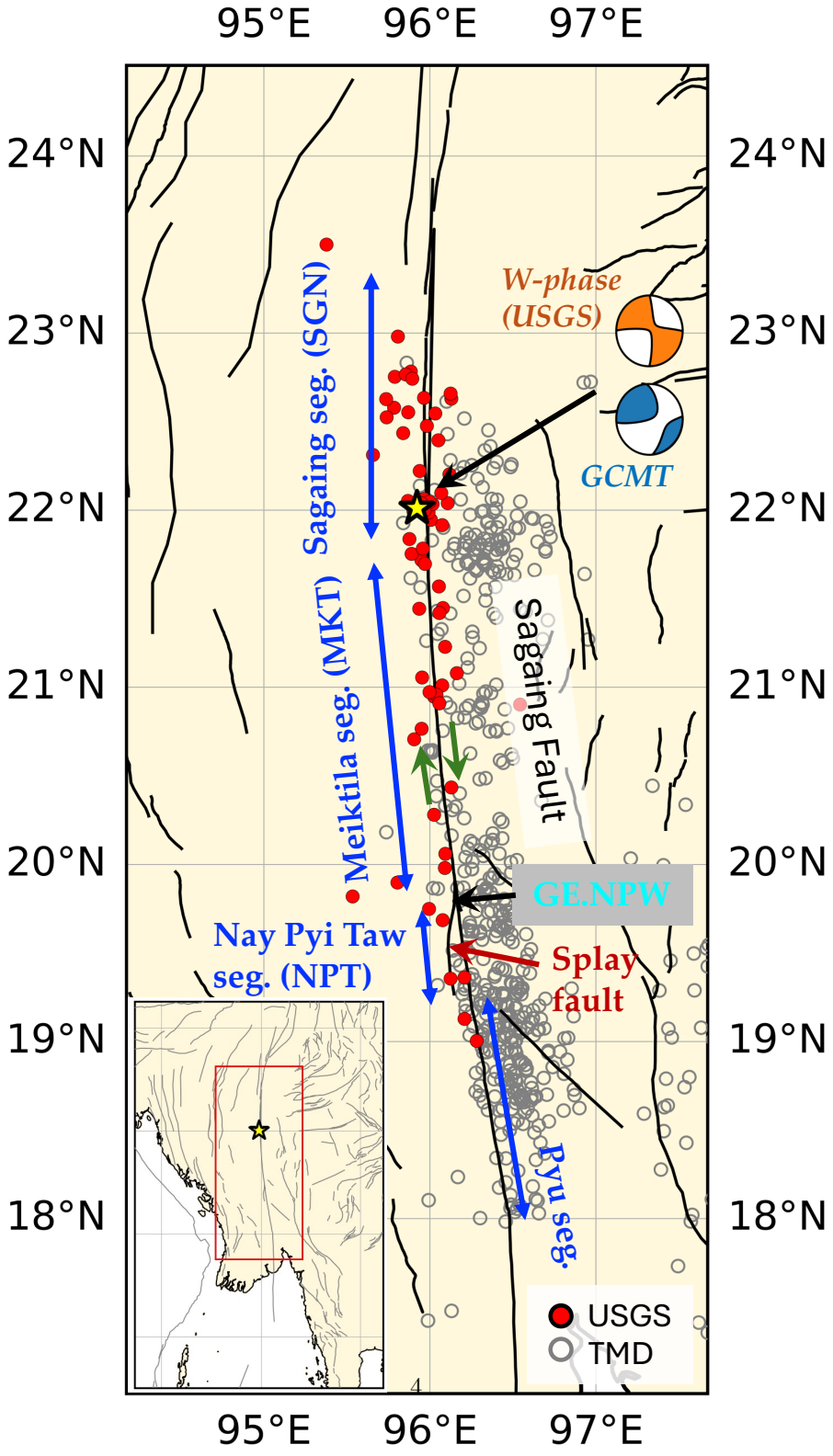

Fig. 1 Map of the study region. The yellow star indicates the epicenter of the Mw 7.7 earthquake on 28 March 2025, and the red dots and gray open circles show aftershocks during the two weeks following the mainshock, cataloged by the USGS and TMD (Thailand Meteorological Department), respectively. The green arrows indicate the relative motion associated with the right-lateral strike-slip fault. The orange and blue focal mechanisms represent the W-phase moment tensor solution (USGS, 2025) and the Global Centroid Moment Tensor solution (GCMT; Dziewonski et al, 1981; Ekström et al, 2012), respectively. The cyan triangle denotes the GEOFON accelerometer station near Nay Pyi Taw (NPT) (GEOFON Data Centre, 1993). Black and gray lines show active fault traces from Styron and Pagani (2020), and segment names follow Wang et al (2014). The inset shows a broader-scale map, with the red rectangle outlining the area shown in the main panel.

supershear regimes based on CCTV observations. Slip models additionally indicate bilateral rupture growth from the epicenter (e.g., Inoue et al, 2025a; Ye et al, 2025; Li et al, 2025; Lindsey et al, 2025). Notably, Inoue et al (2025a) applied a high-degree-of-freedom teleseismic P-wave inversion–the potency density tensor inversion (PDTI)–which allows the fault geometry to vary during inversion (Shimizu et al, 2019; Yamashita et al, 2022), and inferred a boomerang-like back-propagating rupture. Similar back-propagating features were also imaged in BP studies (Vera et al, 2025; Yao et al, 2025), although their physical significance has not been fully discussed, partly due to potential dependence on array geometry and wave type.

Back-propagating rupture (BPR) has been observed during several major earthquakes, including the 2002 Denali (Yamashita et al, 2022), 2011 Tohoku (Ide et al, 2011), 2022 Taiwan (Yagi et al, 2022), and 2023 Kahramanmaraş (Turkey) earthquakes (e.g., Ding et al, 2023; Okuwaki et al, 2023). A comprehensive review by Ding et al (2024) highlighted that BPR can occur during dynamic rupture but is often obscured by dominant radiation from the forward-propagating rupture. They further showed that geometric and structural complexities–such as free-surface reflections, fault bends, asperities, branches, and stepovers (e.g., Ma and Elbanna, 2019; Mia et al, 2024)–can enhance the observability of BPR. Such complexities are commonly associated with enhanced high-frequency seismic radiation (Ding et al, 2024).

For the 2025 Myanmar earthquake, the source region comprises multiple fault segments (Figure 1) (Wang et al, 2014), which may have influenced the rupture evolution (e.g., Bruhat et al, 2016; Gabrieli and Tal, 2025). Inoue et al (2025a) inferred variations in fault strike and dip from teleseismic P-wave data, suggesting spatial variations in fault geometry, including changes in dip angle, consistent with the findings of Ye et al (2025). Sato et al (2025) reconstructed a three-dimensional fault geometry and suggested twisting of the source fault near segment junctions. In addition, a splay fault branches from the junction between the MKT and NPT segments (Wang et al, 2014),

although significant slip on this branch has not been documented in seismological or geodetic studies (e.g., Inoue et al, 2025a; Ye et al, 2025; Yao et al, 2025; Xu et al, 2025). If such spatial variations in fault geometry modulate the rupture progression and arrest, they may generate intense high-frequency P-wave excitation associated with complex rupture phenomena (Adda-Bedia and Madariaga, 2008; Bruhat et al, 2016; Okuwaki and Yagi, 2017; Gabrieli and Tal, 2025; Tarumi and Yoshizawa, 2025).

Despite these advances, it remains unclear (i) what the reported BPRs represent in the context of rupture dynamics and (ii) how spatially varying fault geometry, including segment junctions, fault twisting, and the NPT-adjacent splay fault, affects high-frequency radiation and rupture growth. In this study, we investigate the frequency-dependent P-wave radiation process using multi-frequency teleseismic P-wave BP. By directly comparing the resulting P-wave radiators with the PDTI model of Inoue et al (2025a), we examine the physical interpretation of the observed backward-propagating HF radiation. Moreover, by resolving the contribution of the NPT-adjacent splay fault, we clarify the relationships among high-frequency radiation, back-propagating features, and spatial variations in fault geometry.

2 Data and methods for P-wave back-projection

2.1 Data: Teleseismic P-waves

We collected three-component teleseismic waveform data from EarthScope, removed the instrument response, and converted the records to displacement waveforms. We followed the data-processing workflow of Tarumi and Yoshizawa (2023, 2025) and analyzed three frequency bands: 0.05–0.5 Hz, 0.1–1.0 Hz, and 0.3–2.0 Hz. We restricted the epicentral distance range to 30°–100° for the teleseismic P-wave analysis.

We first applied a cross-correlation-based selection method to the onset window of the teleseismic P-wave, spanning 10 s before and after the reference P-wave arrival

time predicted by the AK135 model (Kennett et al, 1995). We computed the normalized correlation coefficient (NCC) from cross-correlation functions (CCFs) between all waveform pairs and grouped seismograms with NCC > 0.7. The group containing the largest number of traces was selected for the back-projection analysis described in the next subsection. This data-selection scheme was originally developed to extract coherent receiver functions from noisy datasets (Tkalčić et al, 2011) and enables retention of high-quality records with coherent P-wave onsets (Tarumi and Yoshizawa, 2023, 2025).

For the selected group, we used the sign of the NCC to align P-wave polarities to mitigate polarity-related cancellation during waveform stacking. We also derived lag times from the CCFs within the selected group to account for travel-time perturbations caused by three-dimensional heterogeneities and to compensate for P-wave travel-time differences. These procedures were applied independently to each frequency band, thereby reducing multi-scale structural effects on source imaging.

Figures 2 and S1–S2 show the retained P-wave data in each frequency band. The retained datasets provide good azimuthal coverage (Figures 2 and S1–S2 (a)), which helps stabilize the imaging resolution (Fukahata et al, 2014). The azimuthal variations in P-wave train shapes (Figures 2 and S1–S2 (d)) show a coherent impulsive phase at $\sim$20 s at northern stations, which we interpret as a directivity pulse. In contrast, southern stations lack such a pulse and instead exhibit longer wave trains, described as tremor-like by Inoue et al (2025a). These contrasting waveform characteristics likely reflect differences in rupture directivity and source duration. However, previous geophysical studies consistently indicate that the overall rupture propagated predominantly southward (e.g., Li et al, 2025; Lindsey et al, 2025; Ye et al, 2025), which is also consistent with observed radiation patterns of Rayleigh and Love waves (Figure S3). Thus, the tremor-like oscillations at southern stations may represent the stacked

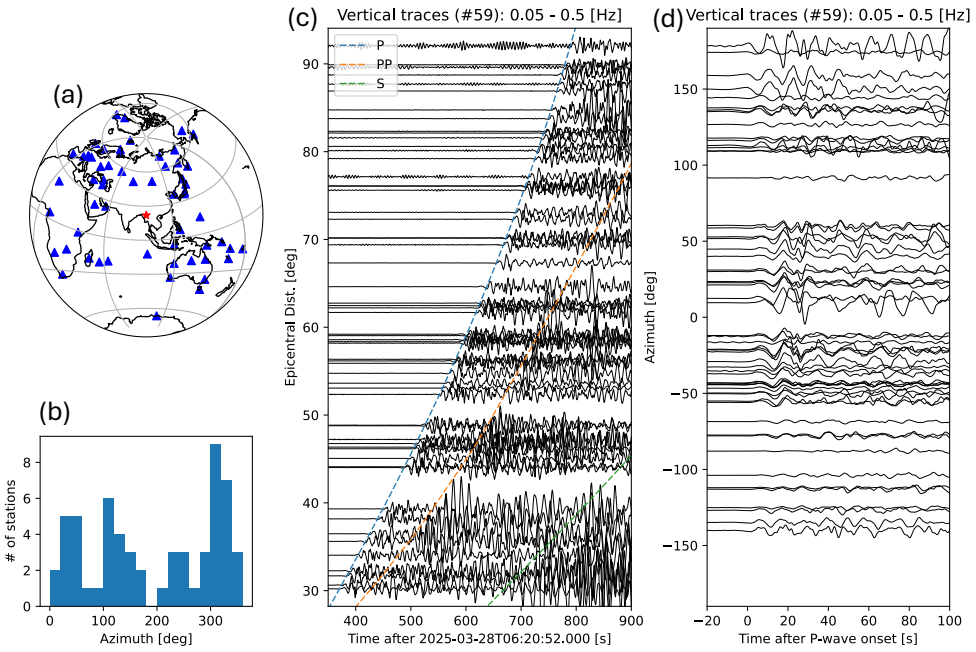

Fig. 2 Teleseismic P-wave dataset for 0.05–0.5 Hz. (a) Station distribution (blue triangles) and the epicenter (red star). (b) Azimuthal distribution of station counts. (c) Vertical-component waveform data sorted by epicentral distance and normalized by the maximum amplitude within each P-wave window. The blue, orange, and green curves indicate the travel-time curves for P, PP, and S phases, respectively. (d) Same as (c), but sorted by station azimuth.

response of the long southward rupture (Inoue et al, 2025a), whereas the impulsive P-waves observed at northern stations are more likely associated with localized rupture phenomena.

2.2 LQT back-projection

We applied the LQT back-projection (BP) method (Tarumi and Yoshizawa, 2025) to image the frequency-dependent P-wave radiation process. The BP method was originally developed by Ishii et al (2005, 2007) to estimate earthquake rupture evolution and has also been used to detect aftershocks hidden by large-earthquake disturbances (Kiser and Ishii, 2013), tsunamis (Mizutani and Yomogida, 2022), and explosive eruption sequences (Tarumi and Yoshizawa, 2023).

The BP method is based on slant stacking, which time-reverses a target phase (e.g., P wave) back to a candidate source region (Figure S4 (a)). In the original BP framework, vertical-component seismograms are often used because teleseismic P-waves are clearly observed on that component. However, teleseismic P-wave energy is partitioned between the vertical and radial (horizontal) components depending on the incident angle at the receiver. We therefore rotated the three-component seismograms into the LQT coordinate system (Figure S4 (b)), which more effectively isolates the incident P-wave motion (in the L component) and is widely used in receiver function studies (e.g., Vinnik, 1977; Kind et al, 2020).

The potential source grid was defined within $\pm 0.75^\circ$ in longitude and from $+1.5^\circ$ to -3.0° in latitude relative to the epicenter (22.001°N, 95.925°E; USGS, 2025). The grid spacing was set to 0.05° for 0.05–0.5 Hz and 0.1–1.0 Hz, and 0.015° for 0.3–2.0 Hz, because a 0.05° spacing is too coarse to resolve the radiation process at the highest frequency range. The incident angles and travel times of P-waves were calculated using the 1-D standard model AK135 (Kennett et al, 1995). For waveform stacking, we employed the N-th root stacking method (Rost and Thomas, 2002) and set $N = 4$ based on trial and error, following Tarumi and Yoshizawa (2025).

3 Results of multi-frequency P-wave back-projections

The resulting BP images are shown in Figure 3. Panels (a–c) present snapshots of the P-wave radiation process for the three frequency bands (a: 0.05–0.5 Hz; b: 0.1–1.0 Hz; c: 0.3–2.0 Hz). Panels (d) and (e) show the temporally and spatially integrated radiation power for each band, respectively. Figure 4 projects the BP images onto the north–south line to display the temporal evolution of P-wave radiation areas, which

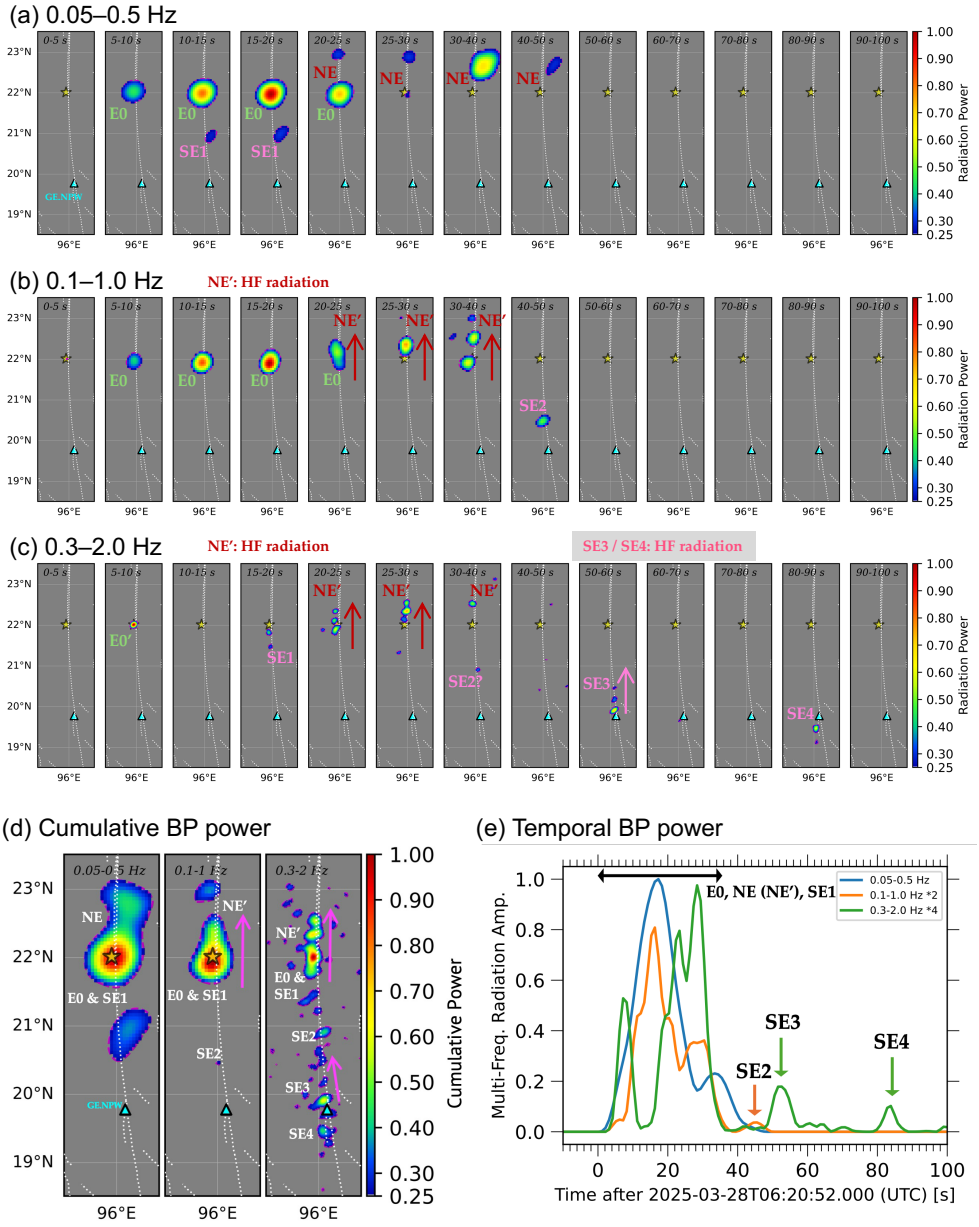

Fig. 3 Summary of multi-frequency BP results. (a-c) Snapshots of BP images for (a) 0.05–0.5 Hz, (b) 0.1–1.0 Hz, (c) 0.3–2.0 Hz. The integration time window is 5 seconds for 0–30 s and 10 seconds for 30–100 s. The yellow star and cyan triangle indicate the epicenter of the Mw 7.7 event and the accelerometer near Nay Pyi Taw (NPT), respectively. White dashed lines represent active fault traces (Styron and Pagani, 2020). For clarity, regions with radiation power lower than 0.25 are masked. Labels E0, NE, and SE correspond to the episode names identified in this study; NE′ denotes the high-frequency dominant feature within the NE episode. Red or pink arrows indicate the migration direction of HF radiators. (d) Time-integrated P-wave radiation power for each frequency band. (e) Temporal radiation power for the three frequency bands; arrows and labels indicate the major episodes. Line colors correspond to the frequency bands, as shown in the legend.

helps quantify the migration speed of P-wave radiators and thus infer the rupture-front propagation speed. In this section, we describe the multi-frequency BP results and compare them with previous seismological inferences for this earthquake.

Our BP results reveal several distinctive episodes associated with bilateral expansion of P-wave radiators (Figure 3 (a–d)). At the beginning, the two low-frequency (LF) bands show moderate P-wave radiation, whereas the high-frequency (HF) band exhibits more impulsive radiation. In Figure 3 (a–c), the HF P-wave radiation appears to emerge earlier than the LF radiation; however, this apparent timing difference should be interpreted cautiously because the LF bands have coarser temporal resolution than the HF band. Nevertheless, the initial emission stage, characterized by relatively intense HF radiation, may reflect the rupture initiation process (E0; Figures 3 (a–c, e) and 4) (Madariaga, 1977, 1983). The E0 episode remains concentrated near the epicenter and becomes the largest P-wave radiation episode, after which the radiating regions expand bilaterally northward and southward (Figure 3 (a–d)), consistent with Yao et al (2025). Most P-wave radiators imaged in our results are located along the mapped active fault traces (Styron and Pagani, 2020).

The southward expansion is imaged as discrete seismic radiation episodes (SE1–SE4; Figures 3 (a–d) and 4). It lasts for about 90 s after initiation, with an average along-fault migration speed of 4–6 km/s. A clear frequency-dependence is evident (Figures 3 (a–d) and 4): SE1 and SE2 are most prominent at 0.05–0.5 Hz and 0.1–1.0 Hz, respectively, whereas SE3 and SE4 are imaged primarily in the highest frequency range (0.3–2.0 Hz). These features are broadly consistent with previously identified P-wave radiators (Yao et al, 2025). These multiple southward radiation episodes may contribute to the tremor-like P-wave trains observed at southern stations (Figures 2, S1, and S2 (c)). The long southward rupture propagation is also consistent with the southward directivity observed in the Rayleigh- and Love-wave amplitudes (Figure S3).

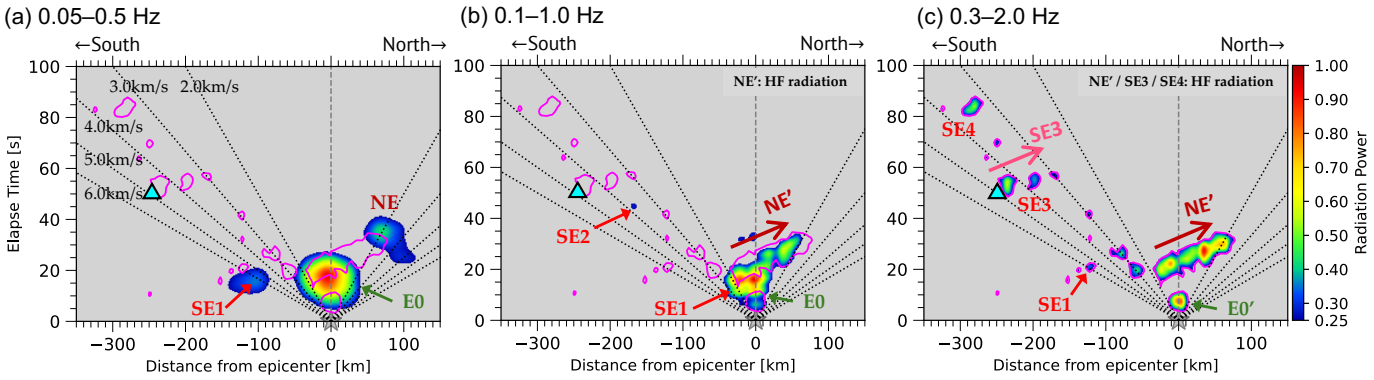

Fig. 4 Time evolution of P-wave radiation projected along the North-South line (a: 0.05–0.5 Hz; b: 0.1–1.0 Hz; c: 0.3–2.0 Hz). Dashed lines represent rupture-front slowness of 2.0–6.0 km/s with 1.0 km/s interval. Magenta contour lines correspond to radiation power of 0.3–2.0 Hz. Cyan triangles denote the location of the accelerometer at Nay Pyi Taw.

SE1 is located approximately 100 km south of the epicenter and occurs 15–20 s after the origin time (OT) (Figures 3 (a) and 4 (a)). Following SE1, although the southern episode cannot be continuously tracked, the next intense P-wave radiation occurs about 200 km south of the epicenter at ∼45 s after OT (SE2; Figures 3 (b) and 4 (b)). After SE2, the P-wave radiation is primarily imaged in the HF band (0.3–2.0 Hz; Figures 3 (c) and 4 (c)). At the final radiation episode captured in this study, SE4, the P-wave radiation is located not on the main fault segment but on the branching splay fault south of NPT (Figures 3 (c) and 4 (c)).

The migration speeds from the epicenter to SE1 and from SE1 to SE2 are estimated to be 6.0–6.5 km/s and 3.0–4.0 km/s, respectively. From SE2 to SE3 during 50–60 s after OT, the P-wave source migrates at ∼ 6.0 km/s along the fault, reaching Nay Pyi Taw (NPT), around 250 km south of the epicenter (Figures 3 (c) and 4 (c)). In addition, northward migration during SE3 occurs at ∼6.0–6.5 km/s, which may reflect a backward-migrating HF radiation episode (Figure 4 (c)). Overall, the temporal variations in migration speed during the Mw 7.7 earthquake may reflect intermittent rupture-speed transitions (Hirano et al, 2025; Latour et al, 2025).

Northward migration is observed at three distinct timings and locations: NE, NE′, and within SE3, where NE′ denotes the HF-dominant feature within the northward-migrating source process. As described above, the third case (SE3) forms part of the southward episode characterized by HF P-wave radiation (Figure 4 (c)). NE and NE′ occur within the Sagaing segment; NE is observed near the northern tip of the segment (Figures 3 (a) and 4 (a)), whereas NE′ corresponds to the largest northward radiation episode identified in the HF bands (Figures 3 and 4). NE is generated at 20–30 s after OT, implying a rupture-front propagation speed of 3.0–4.0 km/s (Figures 3 (a) and 4 (a)). NE may represent the northward component of bilateral rupture growth (Inoue et al, 2025a), part of NE′, or overlapping contributions from both processes. Given the limited spatiotemporal resolution of teleseismic BP, these possibilities cannot be uniquely distinguished in the present analysis. For NE′, rapid northward migration of HF P-wave radiators is observed from the southern tip of the Sagaing segment (Figures 3 (b, c) and 4 (b, c)), potentially reflecting backward-migrating HF radiation. This pronounced episode likely contributes to the observed directivity pulses at the northern seismic stations (Figures 2 and S1–S2).

4 Near-field seismic records at Nay Pyi Taw

4.1 Near-field strong-motion data

Three-component strong-motion data recorded at Nay Pyi Taw provide key constraints on the rupture process of this Mw 7.7 earthquake. Because the NS component is nearly parallel to the fault strike direction ($\sim$ 350°–360°), we did not rotate the horizontal components. Compared with acceleration seismograms, velocity and displacement waveforms provide more direct information about the fault-rupture process. In particular, the onset of quasi-static displacement enables estimation of the average rupture velocity. During time integration, we applied baseline drift correction using a median

filter method developed by Watanabe et al (2021). The correction strategy is briefly explained in Text S1 in the supplementary material.

Figure 5 shows the acceleration, velocity, and displacement waveforms. In Figure 5 (a), the vertical component contains larger portions of high-frequency energy, whereas prominent low-frequency signals follow the high-frequency arrivals in the two horizontal components. In the velocity records (Figure 5 (b)), the two horizontal components indicate prominent low-frequency pulses, particularly in the NS component, which is nearly parallel to the fault motion. The displacement records (Figure 5 (c)) are also dominated by larger amplitude in the NS component and show a static offset of ~ 1.6 m, which is consistent with earlier estimates (Ye et al, 2025; Vera et al, 2025; Xu et al, 2025) and geodesic observations (Melgar et al, 2025; Xu et al, 2025).

4.2 Interpretations of near-field records in comparison with BP results

The pronounced positive velocity pulse and associated displacement in the NS component reflect quasi-static fault slip, reaching a peak displacement of $\sim$2.2 m. The onset of this displacement occurs approximately 50–52 s after OT, suggesting an average rupture velocity of 4.5–5.0 km/s between the epicenter and GE.NPW (Figure 5 (b, c)). This estimate matches well with the timing of SE3 identified in our BP results (Figure 3 (c–e)). In addition to the fault-motion signal, high-frequency waves arrive within the SE3 time window, supporting the interpretation that HF radiation was particularly prominent at this stage.

The rise time of the main pulse is at most 3 s (Figure 5), consistent with Kearse and Kaneko (2025). Significant negative offsets and velocity pulses immediately follow the ramp-shaped displacement associated with fault motion (Figure 5). This feature is not evident in CCTV-based near-field observations at other locations (Kearse and Kaneko, 2025; Latour et al, 2025; Hirano et al, 2025). By reproducing the observed

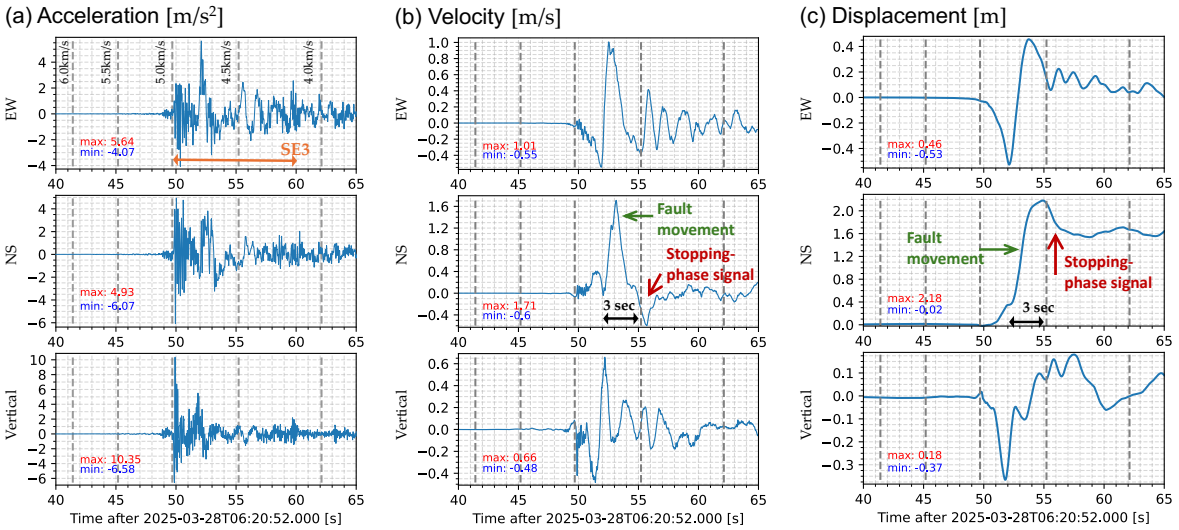

Fig. 5 Strong-motion records at the Nay Pyi Taw station (GE.NPW): (a) acceleration, (b) velocity, and (c) displacement. In each panel, the maximum and minimum amplitudes are indicated by red and blue labels, respectively. Vertical gray lines mark the predicted arrival time of the rupture front, assuming propagation speeds of 4–6 km/s at 0.5 km/s intervals. The orange arrow in the upper-left panel indicates the duration of the episode SE3 that radiates high-frequency P-waves. Green arrows indicate a phase associated with fault motion, and black arrows denote their duration. Red arrows highlight signals potentially associated with the near-field response to abrupt rupture deceleration north of the station.

waveforms using dynamic rupture simulations, Ding et al (2025) demonstrated that this negative velocity pulse can be attributed to a stopping phase. Kearse and Kaneko (2026) more recently reported that the negative phase immediately following the static offset reflects the stopping phase of fault slip. Our BP results capture intense HF P-wave radiation near GE.NPW (SE3; Figures 3 (c, d) and 4 (c)), consistent with theoretical predictions of stopping-phase radiation generated by abrupt rupture termination (Savage, 1965; Madariaga, 1977). Thus, the prominent negative phases at the NS component (Figure 5 (b, c)) can be interpreted as near-field signatures of a stopping phase.

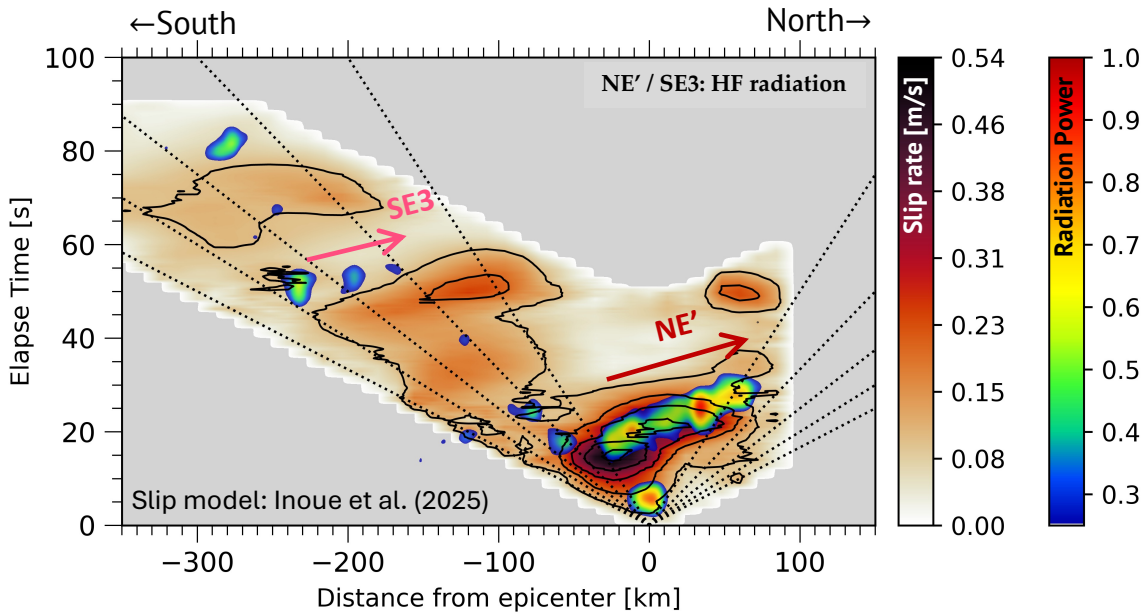

Fig. 6 Comparison between our BP model (0.3–2.0 Hz) and the slip model of Inoue et al (2025a). The format is similar to Figure 4 (c), but the background color contours represent slip rate with contour intervals of 0.1 m/s.

5 Discussion

Our frequency-dependent teleseismic back-projection (BP) results highlight two key aspects of complex rupture behavior during the 2025 Myanmar earthquake: (i) backward-migrating high-frequency (HF) radiation initiated at major segment junctions (NE′ and SE3), and (ii) intense HF radiators on a short splay-fault branch near Nay Pyi Taw (NPT) (SE4). We discuss how these features relate to fault geometry and rupture kinematics in light of previous theoretical and experimental studies.

A primary feature of our BP results is the observation of backward-migrating HF radiators at the Sagaing–Meiktila (SGN–MKT) and MKT–NPT junctions, labeled NE′ and SE3 (Figures 3 (b, c) and 4). This behavior is consistent with several independent source models of the 2025 Myanmar earthquake (e.g., Inoue et al, 2025a;

Sato et al, 2025; Vera et al, 2025; Xu et al, 2025). Figure 6 compares our HF P-wave radiation (0.3–2.0 Hz) with the slip model of Inoue et al (2025a), showing that backward-migrating HF radiators are located near both the SGN–MKT junction (NE$'$) and the MKT–NPT junction (SE3). NE$'$ is located approximately 40–50 km south of the epicenter, near the junction between the SGN and MKT segments (Wang et al, 2014). SE3 occurs in a structurally complex region where rupture may bifurcate onto the splay fault while continuing along the main NPT segment. These backward-migrating HF radiators migrate at apparent speeds of 6.0–6.5 km/s, comparable to local P-wave velocities (Laske et al, 2013) and consistent with earlier BP and kinematic models (Vera et al, 2025; Inoue et al, 2025a) (Figures 6 (b–d) and 4 (b, c)). Interestingly, NE$'$ and SE3 exhibit similar apparent migration speeds. Although this similarity may suggest a common underlying physical control, our present analysis does not allow us to identify the specific mechanism responsible for it. Dynamic rupture simulations and laboratory experiments (Bruhat et al, 2016; Ma and Elbanna, 2019; Ding et al, 2024; Mia et al, 2024; Gabrieli and Tal, 2025) demonstrate that geometric complexities, such as bends, junctions, and branching, can promote complex rupture behaviors, including supershear rupture and associated stopping phases, providing a plausible mechanism for the observed NE$'$ and SE3 episodes.

5.1 Rupture on the splay fault

Our BP results identify an intense HF radiation episode (SE4) on a short splay-fault branch near the NPT segment (Figures 3 (c, d) and 4). InSAR observations indicate that this splay fault contributes only modestly to the overall coseismic deformation compared with the main fault trace (e.g., Xu et al, 2025; Li et al, 2025; Lindsey et al, 2025). Accordingly, most finite-fault inversions did not explicitly incorporate this splay fault in their parameterized geometries and therefore did not resolve significant slip on it (e.g., Inoue et al, 2025a; Xu et al, 2025; Ye et al, 2025; Sato et al, 2025).

Nevertheless, several teleseismic BP studies consistently identified HF radiators near the splay fault (Xu et al, 2025; Ye et al, 2025; Vera et al, 2025; Yao et al, 2025). In particular, Yao et al (2025) employed a multi-frequency BP approach similar to ours and found that HF radiation (0.2–2.0 Hz) preferentially illuminates the splay fault.

Teleseismic P-wave-based analyses do not indicate strong radiation from the southern NPT segment (e.g., Inoue et al, 2025a; Ye et al, 2025; Vera et al, 2025; Sato et al, 2025), whereas joint inversions incorporating geodetic data and additional seismic phases (e.g., surface waves) estimate meter-scale slip patches (typically 1–3 m) in this region (e.g., Xu et al, 2025; Melgar et al, 2025; Lindsey et al, 2025). This discrepancy likely reflects the limited resolving power of teleseismic P waves for near-vertical strike-slip fault ruptures due to their radiation pattern, as many teleseismic stations lie close to the nodal directions of P-wave radiation. A similar limitation was noted by Yao et al (2025) through comparisons with regional Rayleigh-wave BP results.

This splay fault corresponds to a releasing bend in an overall right-lateral strike-slip system (Wang et al, 2014), which may facilitate rupture propagation from the main fault onto the branching fault (e.g., Gabrieli and Tal, 2025). In addition, a bimaterial contrast across the main fault may also contribute to activation of the branching fault. A recent travel-time tomography of the source region revealed a pronounced velocity contrast across the Sagaing Fault and imaged the western side as a significant low-velocity anomaly (Zhang et al, 2026), suggesting that the splay fault lies within or adjacent to relatively compliant material. Such an environment may facilitate rupture on the splay fault (DeDontney et al, 2011), as well as the supershear rupture along the main fault (e.g., Yao et al, 2025; Xu et al, 2025).

In contrast, HF P-waves are sensitive to rapid, localized changes in rupture kinematics and are therefore well suited to capturing complex features such as radiation from the short splay fault (e.g., Xu et al, 2025; Yao et al, 2025). The limited HF radiation along the southern NPT segment (Figures 3 (c, d); e.g., Vera et al (2025); Yao

et al (2025); Xu et al (2025)) may suggest smoother deceleration and/or spontaneous rupture arrest (Bizzarri et al, 2010). The aftershock distribution around the junction shows a distinctive pattern: the MKT segment hosts relatively few earthquakes, whereas localized clusters appear near NPT. Such clustering is not evident in the seismicity prior to the Mw 7.7 event (Figure S5). Together with a relatively small slip near the junction inferred from kinematic models (Inoue et al, 2025a; Ye et al, 2025; Li et al, 2025; Lindsey et al, 2025), this pattern may indicate locally different stress conditions near NPT (e.g., relatively low stress drop or barrier-like condition), which could be linked to rupture arrest at the MKT–NPT junction.

5.2 Backward-migrating HF radiation and the role of fault geometry

A plausible interpretation of SE3 is that it represents a stopping phase whose radiation appears as backward-migrating HF radiators in our BP images. Ding et al (2025) and Kearse and Kaneko (2026) associated the negative velocity pulse in the nearly fault-parallel NS component (Figure 5) with a northward-propagating stopping phase. Consistently, SE3 in our BP results is characterized by strong HF radiation (Figures 3 (c,d)), a typical character of stopping phases (Savage, 1965; Madariaga, 1977). In addition, HF radiators during SE3 are preferentially located near the edges of high slip-rate patches (Figure 6). Together, these observations indicate that SE3 likely reflects a stopping phase whose radiation appears as backward migration in BP images, associated with the complex junction near Nay Pyi Taw. Similar characteristics are observed for NE$'$, which also initiates near the SGN–MKT junction (Figure 3 (c, d)) and is concentrated along the edges of high slip-rate patches (Figure 6).

Both episodes of backward-migrating HF radiation originate near major fault junctions at SGN–MKT and MKT–NPT (Figure 3 (c, d)). Laboratory experiments and dynamic rupture simulations demonstrate that geometric irregularities, such as bends

(e.g., Ding et al, 2024), branches (e.g., Ma and Elbanna, 2019), and stepovers (e.g., Mia et al, 2024), can promote supershear rupture and associated stopping-phase radiation.

The SGN–MKT junction is characterized by variations in fault dip and possible twisting of the fault geometry (Inoue et al, 2025a; Sato et al, 2025; Ye et al, 2025). Such a restraining configuration can promote supershear transition (Gabrieli and Tal, 2025), trigger stopping phases (Ding et al, 2024), and locally reduce slip rate (e.g., Inoue et al, 2025a; Lindsey et al, 2025; Ye et al, 2025) and rupture speed (Hirano et al, 2025), consistent with the observed NE$'$ episode.

In contrast, the MKT–NPT junction is more consistent with a releasing bend in an overall right-lateral strike-slip system (Wang et al, 2014). A simple bend alone is therefore unlikely to explain the SE3 episode (Gabrieli and Tal, 2025). Instead, rupture branching onto the short splay fault (Figures 3 (c, d); Section 5.1) likely played a key role. Fault branching has been shown to promote supershear rupture and associated stopping-phase radiation, and facilitate rupture arrest on the main fault (Ma and Elbanna, 2019). This interpretation is consistent with the SE3-SE4 sequence and the limited HF radiation farther south along the NPT segment.

Other factors may also contribute to the generation of backward-migrating stopping phases, including potential variations in local stress conditions and fault-zone structure. A focal mechanism transition near the MKT–NPT junction appears less likely for the Mw 7.7 event, because finite-fault models consistently favor strike-slip faulting (e.g., Xu et al, 2025; Inoue et al, 2025a; Ye et al, 2025), despite a historical thrust-type event in the broader region (Tun and Watkinson, 2017). In contrast, the localized seismicity near NPT (Figure S5) and the relatively small slip inferred near the junction region in several kinematic models (e.g., Inoue et al, 2025a; Li et al, 2025; Lindsey et al, 2025) may be consistent with spatially heterogeneous stress conditions, which could facilitate abrupt rupture arrest. Near the SGN–MKT junction, we can

also observe a similar pattern in seismicity (Figure 1 and S5) and coseismic slip distributions (e.g., Inoue et al, 2025a; Lindsey et al, 2025; Li et al, 2025). Additionally, Hirano et al (2025) suggested a local decrease in rupture speed. These observations are consistent with the idea that local stress contrasts can modulate rupture termination and the generation of backward-migrating stopping phases.

Overall, the observed backward-migrating HF radiation can be primarily interpreted as geometric effects of the segmented fault system, in which junctions and branching structures modulate rupture deceleration, arrest, and associated HF radiation. Such geometrical effects may be further influenced by local properties of the source region (e.g., bimaterial contrast) and spatially heterogeneous stress conditions suggested by localized seismicity and several kinematic models. These geometric complexities, combined with local material contrasts and heterogeneous prestress conditions, may enable backward-migrating P-wave pulses associated with stopping phases that would otherwise be obscured by dominant forward rupture propagation.

6 Conclusions

In this paper, we imaged the frequency-dependent P-wave radiation process using multi-frequency teleseismic back-projection (BP) and compared it with near-field strong-motion records at Nay Pyi Taw (GE.NPW) to investigate the complex rupture behavior of the 2025 Mw 7.7 Myanmar earthquake. Our main conclusions are as follows:

1. Frequency-dependent BP images reveal episodes of backward-migrating high-frequency (HF) radiation (NE$'$ and SE3) initiated near major segment junctions (Figures 3 and 4). These signals migrate at apparent speeds of 6.0–6.5 km/s, comparable to local P-wave velocities.
2. The spatial concentration of HF radiators near the edges of high slip-rate patches (Figure 6), together with the negative velocity pulse observed in near-field records

at GE.NPW (Figure 5), suggests that these backward-migrating HF radiators represent stopping-phase radiation associated with abrupt rupture deceleration.

3. Geometric complexities, including major segment junctions and rupture branching onto a short splay fault, likely played a key role in modulating rupture deceleration, arrest, and associated HF radiation. These structural features, potentially enhanced by the bimaterial effect and local stress state, may explain the observed backward-migrating stopping-phase pulses.

Acknowledgment

We are grateful to the Editor, Eiichi Fukuyama, and two anonymous reviewers for their constructive comments, which helped improve the original manuscript. All seismograms used in this study were downloaded from the EarthScope Data Management Center (https://ds.iris.edu/ds/nodes/dmc/). We used ObsPy (Beyreuther et al, 2010) for downloading and analyzing seismic waveform data. Figures were generated using matplotlib (Hunter, 2007), cartopy (Met Office, 2010), Generic Mapping Tools (Wessel et al, 2019), and PyGMT (Uieda et al, 2021). We visualized Figure 6 using the published model dataset of Inoue et al (2025b). We thank Prof. Ryo Okuwaki (University of Tsukuba) and Dr. Ritsuya Shibata (National Research Institute for Earth Science and Disaster Resilience) for constructive discussions and encouragement that helped improve this study.

Data Availability

All seismic waveform data used in this study are available from the EarthScope Data Management Center (https://ds.iris.edu/ds/nodes/dmc/). The networks used in this study are: II (Scripps Institution of Oceanography, 1986); IU (Albuquerque Seismological Laboratory/USGS, 1988); G (Institut de physique du globe de Paris (IPGP) and École et Observatoire des Sciences de la Terre de Strasbourg (EOST), 1982); IC

(Albuquerque Seismological Laboratory/USGS, 1982); GE (GEOFON Data Centre, 1993).

Competing Interests

The authors declare that they have no competing financial or non-financial interests.

Author Contributions

KT: Conceptualization, Data curation, Methodology, Formal analysis, Funding acquisition, Investigation, Visualization, Project Administration, Software, Writing - Original draft, Writing – review and editing; KY: Conceptualization, Funding acquisition, Investigation, Project Administration, Writing – review and editing

References

Adda-Bedia M, Madariaga R (2008) Seismic radiation from a kink on an antiplane FaultSeismic radiation from a kink on an antiplane fault. Bulletin of the Seismological Society of America 98(5):2291–2302. https://doi.org/10.1785/0120080003

Albuquerque Seismological Laboratory/USGS (1982) New china digital seismograph network. URL https://www.fdsn.org/networks/detail/IC/

Albuquerque Seismological Laboratory/USGS (1988) Global seismograph network (gsn - iris/usgs). https://doi.org/10.7914/SN/IU, URL https://www.fdsn.org/networks/detail/IU/

Beyreuther M, Barsch R, Krischer L, et al (2010) ObsPy: A python toolbox for seismology. Seismological Research Letters 81(3):530–533. https://doi.org/10.1785/gssrl.81.3.530

Bizzarri A, Dunham EM, Spudich P (2010) Coherence of mach fronts during heterogeneous supershear earthquake rupture propagation: Simulations and comparison with observations. Journal of Geophysical Research: Solid Earth 115(B8). https://doi.org/10.1029/2009jb006819

Bruhat L, Fang Z, Dunham EM (2016) Rupture complexity and the supershear transition on rough faults. Journal of Geophysical Research: Solid Earth 121(1):210–224. https://doi.org/10.1002/2015jb012512

DeDontney N, Rice JR, Dmowska R (2011) Influence of material contrast on fault branching behavior. Geophysical Research Letters 38(14). https://doi.org/10.1029/2011gl047849

Ding X, Xu S, Xie Y, et al (2023) The sharp turn: Backward rupture branching during the 2023 mw 7.8 kahramanmaraş (türkiye) earthquake. Seismica 2(3). https://doi.org/10.26443/seismica.v2i3.1083

Ding X, Xu S, Fukuyama E, et al (2024) Back-propagating rupture: Nature, excitation, and implications. Journal of Geophysical Research: Solid Earth 129(10). https://doi.org/10.1029/2024jb029629, 2406.01286

Ding X, Xu S, Ye L (2025) Intermittent supershear rupture punctuated by barrier-induced stopping phase during the 2025 mw 7.8 myanmar earthquake: Evidence from near-fault strong motion observation. Geophysical Research Letters 52(23). https://doi.org/10.1029/2025gl118863

Dziewonski AM, Chou T, Woodhouse JH (1981) Determination of earthquake source parameters from waveform data for studies of global and regional seismicity. Journal of Geophysical Research: Solid Earth 86(B4):2825–2852. https://doi.org/10.1029/jb086ib04p02825

Ekström G, Nettles M, Dziewoński A (2012) The global CMT project 2004–2010: Centroid-moment tensors for 13,017 earthquakes. Physics of the Earth and Planetary Interiors 200:1–9. https://doi.org/10.1016/j.pepi.2012.04.002

Fukahata Y, Yagi Y, Rivera L (2014) Theoretical relationship between back-projection imaging and classical linear inverse solutions. Geophysical Journal International 196(1):552–559. https://doi.org/10.1093/gji/ggt392

Gabrieli T, Tal Y (2025) Lab earthquakes reveal a wide range of rupture behaviors controlled by fault bends. Proceedings of the National Academy of Sciences of the United States of America 122(17):e2425471122. https://doi.org/10.1073/pnas.2425471122

GEOFON Data Centre (1993) GEOFON seismic network. URL http://geofon.gfz-potsdam.de/doi/network/GE

Hirano S, Doke R, Maeda T (2025) Supershear-subshear-supershear rupture sequence during the 2025 mandalay earthquake in myanmar. Seismica 4(2). https://doi.org/10.26443/seismica.v4i2.1785

Hunter JD (2007) Matplotlib: A 2d graphics environment. Computing in Science & Engineering 9(3):90–95. https://doi.org/10.1109/mcse.2007.55

Hurukawa N, Maung PM (2011) Two seismic gaps on the sagaing fault, myanmar, derived from relocation of historical earthquakes since 1918. Geophysical Research Letters 38(1):n/a–n/a. https://doi.org/10.1029/2010gl046099

Ide S, Baltay A, Beroza GC (2011) Shallow dynamic overshoot and energetic deep rupture in the 2011 mw 9.0 tohoku-oki earthquake. Science 332(6036):1426–1429. https://doi.org/10.1126/science.1207020

Inoue N, Yamaguchi R, Yagi Y, et al (2025a) A multiple asymmetric bilateral rupture sequence derived from the peculiar tele-seismic p-waves of the 2025 mandalay, myanmar earthquake. Seismica 4(1). https://doi.org/10.26443/seismica.v4i1.1691

Inoue N, Yamaguchi R, Yagi Y, et al (2025b) Archive of pdti models for the 2025 myanmar earthquake. https://doi.org/10.5281/zenodo.15386684, URL https://doi.org/10.5281/zenodo.15386684

Institut de physique du globe de Paris (IPGP), École et Observatoire des Sciences de la Terre de Strasbourg (EOST) (1982) Geoscope, french global network of broad band seismic stations. https://doi.org/10.18715/GEOSCOPE.G, URL http://geoscope.ipgp.fr/networks/detail/G/

Ishii M, Shearer PM, Houston H, et al (2005) Extent, duration and speed of the 2004 sumatra–andaman earthquake imaged by the hi-net array. Nature 435(7044):933–936. https://doi.org/10.1038/nature03675

Ishii M, Shearer PM, Houston H, et al (2007) Teleseismic p wave imaging of the 26 december 2004 sumatra-andaman and 28 march 2005 sumatra earthquake ruptures using the hi-net array. Journal of Geophysical Research: Solid Earth (1978–2012) 112(B11). https://doi.org/10.1029/2006jb004700

Kearse J, Kaneko Y (2025) Curved fault slip captured by CCTV video during the 2025 mw 7.7 myanmar earthquake. The Seismic Record 5(3):281–288. https://doi.org/10.1785/0320250024

Kearse J, Kaneko Y (2026) Stopping phase reveals abrupt arrest of large strike-slip earthquakes. Science https://doi.org/10.1126/science.aef3733

Kennett BLN, Engdahl ER, Buland R (1995) Constraints on seismic velocities in the earth from traveltimes. Geophysical Journal International 122(1):108–124. https:

//doi.org/10.1111/j.1365-246x.1995.tb03540.x

Kind R, Mooney WD, Yuan X (2020) New insights into the structural elements of the upper mantle beneath the contiguous united states from s-to-p converted seismic waves. Geophysical Journal International https://doi.org/10.1093/gji/ggaa203

Kiser E, Ishii M (2013) Hidden aftershocks of the 2011 mw 9.0 tohoku, japan earthquake imaged with the backprojection method. Journal of Geophysical Research: Solid Earth 118(10):5564–5576. https://doi.org/10.1002/2013jb010158

Laske G, Masters G, Ma Z, et al (2013) Update on CRUST1.0 - a 1-degree global model of earth's crust. URL https://igppweb.ucsd.edu/~gabi/rem.html

Latour S, Lebihain M, Bhat HS, et al (2025) Direct estimation of earthquake source properties from a single CCTV camera. Science 390(6772):463–467. https://doi.org/10.1126/science.adz1705

Li B, Jónsson S, Suhendi C, et al (2025) Seismic gap breached by the 2025 mw 7.7 mandalay (myanmar) earthquake. Nature Geoscience pp 1–9. https://doi.org/10.1038/s41561-025-01861-7

Lindsey EO, Kuo YT, Wang Y, et al (2025) Mature fault mechanics revealed by the highly efficient 2025 mandalay earthquake. Nature Communications 16(1):10937. https://doi.org/10.1038/s41467-025-65942-2

Ma X, Elbanna A (2019) Dynamic rupture propagation on fault planes with explicit representation of short branches. Earth and Planetary Science Letters 523:115702. https://doi.org/10.1016/j.epsl.2019.07.005

Madariaga R (1977) High-frequency radiation from crack (stress drop) models of earthquake faulting. Geophysical Journal of the Royal Astronomical Society

51(3):625–651. https://doi.org/10.1111/j.1365-246x.1977.tb04211.x

Madariaga R (1983) High frequency radiation from dynamic earthquake fault models. Annales de Geophysique 1(1):17–23. URL http://inis.iaea.org/search/search.aspx?orig_q=RN:14783441

Melgar D, Weldon R, Wang Y, et al (2025) Supershear source model of the 2025 m7.8 myanmar earthquake and paleoseismology of the sagaing fault: regions of significant overlap with past earthquakes. Seismica 4(2). https://doi.org/10.26443/seismica.v4i2.1771

Met Office (2010) Cartopy: a cartographic python library with a matplotlib interface. URL https://scitools.org.uk/cartopy

Mia MS, Abdelmeguid M, Harris RA, et al (2024) Rupture jumping and seismic complexity in models of earthquake cycles for fault stepovers with off-fault plasticity. Bulletin of the Seismological Society of America 114(3):1466–1480. https://doi.org/10.1785/0120230249

Mizutani A, Yomogida K (2022) Back-projection imaging of a tsunami excitation area with ocean-bottom pressure gauge array data. Journal of Geophysical Research: Oceans https://doi.org/10.1029/2022jc018480

Okuwaki R, Yagi Y (2017) Role of geometric barriers in irregular-rupture evolution during the 2008 wenchuan earthquake. Geophysical Journal International 212(3):1657–1664. https://doi.org/10.1093/gji/ggx502

Okuwaki R, Yagi Y, Taymaz T, et al (2023) Multi-scale rupture growth with alternating directions in a complex fault network during the 2023 south-eastern türkiye and syria earthquake doublet. Geophysical Research Letters 50(12). https://doi.org/10.1029/2023gl103480

Rost S, Thomas C (2002) ARRAY SEISMOLOGY: METHODS AND APPLICATIONS: ARRAY SEISMOLOGY. Reviews of Geophysics 40(3):2–1–2–27. https://doi.org/10.1029/2000rg000100

Sato D, Ryo O, Yagi Y, et al (2025) Strike-slip restraining screwed fault geometry reconstructed from the 2025 myanmar earthquake. arXiv, preprint https://doi.org/10.31223/x5xx6c

Savage JC (1965) The stopping phase on seismograms. Bulletin of the Seismological Society of America 55(1):47–58. https://doi.org/10.1785/bssa0550010047

Scripps Institution of Oceanography (1986) Global seismograph network - iris/ida. https://doi.org/10.7914/SN/II, URL https://www.fdsn.org/networks/detail/II/

Shimizu K, Yagi Y, Okuwaki R, et al (2019) Development of an inversion method to extract information on fault geometry from teleseismic data. Geophysical Journal International 220(2):1055–1065. https://doi.org/10.1093/gji/ggz496

Styron R, Pagani M (2020) The GEM global active faults database. Earthquake Spectra 36(1_suppl):160–180. https://doi.org/10.1177/8755293020944182

Tarumi K, Yoshizawa K (2023) Eruption sequence of the 2022 hunga tonga-hunga ha'apai explosion from back-projection of teleseismic p waves. Earth and Planetary Science Letters 602:117966. https://doi.org/10.1016/j.epsl.2022.117966

Tarumi K, Yoshizawa K (2025) Frequency-dependent seismic radiation process of the 2024 noto peninsula earthquake from teleseismic p-wave back-projection. Earth and Planetary Science Letters 666:119509. https://doi.org/10.1016/j.epsl.2025.119509

Tkalčić H, Chen Y, Liu R, et al (2011) Multistep modelling of teleseismic receiver functions combined with constraints from seismic tomography: crustal structure

beneath southeast china. Geophysical Journal International 187(1):303–326. https://doi.org/10.1111/j.1365-246x.2011.05132.x

Tun ST, Watkinson IM (2017) Chapter 19 the sagaing fault, myanmar. Geological Society, London, Memoirs 48(1):413–441. https://doi.org/10.1144/m48.19

Uieda L, Tian D, Leong WJ, et al (2021) PyGMT: A python interface for the generic mapping tools. https://doi.org/10.5281/zenodo.5607255, URL https://doi.org/10.5281/zenodo.5607255

USGS (2025) M 7.7 - 2025 mandalay, burma (myanmar) earthquake. URL https://earthquake.usgs.gov/earthquakes/eventpage/us7000pn9s/executive

Vera F, Carrillo-Ponce A, Crosetto S, et al (2025) Supershear rupture along the sagaing fault seismic gap: The 2025 myanmar earthquake. The Seismic Record 5(3):289–299. https://doi.org/10.1785/0320250025

Vinnik L (1977) Detection of waves converted from p to SV in the mantle. Physics of the Earth and Planetary Interiors 15(1):39–45. https://doi.org/10.1016/0031-9201(77)90008-5, URL https://www.sciencedirect.com/science/article/pii/0031920177900085

Wang Y, Sieh K, Tun ST, et al (2014) Active tectonics and earthquake potential of the myanmar region. Journal of Geophysical Research: Solid Earth 119(4):3767–3822. https://doi.org/10.1002/2013jb010762

Watanabe T, Komatsu M, Takenaka H (2021) Estimation of displacement waveforms by baseline correction of near-fault acceleration records of the 2016 kumamoto earthquake with median filter (in japanese with english abstract). Okayama University Earth Science Report https://doi.org/10.18926/esr/61959, URL http://doi.org/10.18926/ESR/61959

Wessel P, Luis JF, Uieda L, et al (2019) The generic mapping tools version 6. Geochemistry, Geophysics, Geosystems 20(11):5556–5564. https://doi.org/10.1029/2019gc008515

Xu L, Meng L, Yunjun Z, et al (2025) Bimaterial effect and favorable energy ratio enabled supershear rupture in the 2025 mandalay earthquake. Science 390(6772):476–481. https://doi.org/10.1126/science.ady6100

Yagi Y, Okuwaki R, Enescu B, et al (2022) Irregular rupture process of the 2022 taitung, taiwan, earthquake sequence. Scientific reports 13(1):1107. https://doi.org/10.1038/s41598-023-27384-y

Yamashita S, Yagi Y, Okuwaki R, et al (2022) Potency density tensor inversion of complex body waveforms with time-adaptive smoothing constraint. Geophysical Journal International 231(1):91–107. https://doi.org/10.1093/gji/ggac181

Yao Q, Yu C, Zhou M (2025) Bilateral supershear rupture of the 2025 MW 7.7 myanmar earthquake imaged by global p-wave and regional surface-wave back-projections. Geophysical Research Letters 52(20). https://doi.org/10.1029/2025gl116800

Ye L, Lay T, Kanamori H (2025) The 28 march 2025 mw 7.8 myanmar earthquake: Preliminary analysis of an 480km long intermittent supershear rupture. The Seismic Record 5(3):260–269. https://doi.org/10.1785/0320250021

Zhang F, Li Y, Chen Y (2026) Velocity structure of the 2025 mw7.7 myanmar earthquake source region: Insights from traveltime reciprocity tomography. Tectonophysics 918:230985. https://doi.org/10.1016/j.tecto.2025.230985

Supplementary Material for

Role of Fault Geometry in Generating Backward-migrating P-wave Radiation During the 2025 Mw 7.7 Myanmar Earthquake

K. Tarumi[1,*] and K. Yoshizawa[1]

[1] Department of Earth & Planetary Sciences, Faculty of Science, Hokkaido University, Sapporo 060-0810, Japan.

[*]Corresponding author: tarumi.kotaro.jp@gmail.com

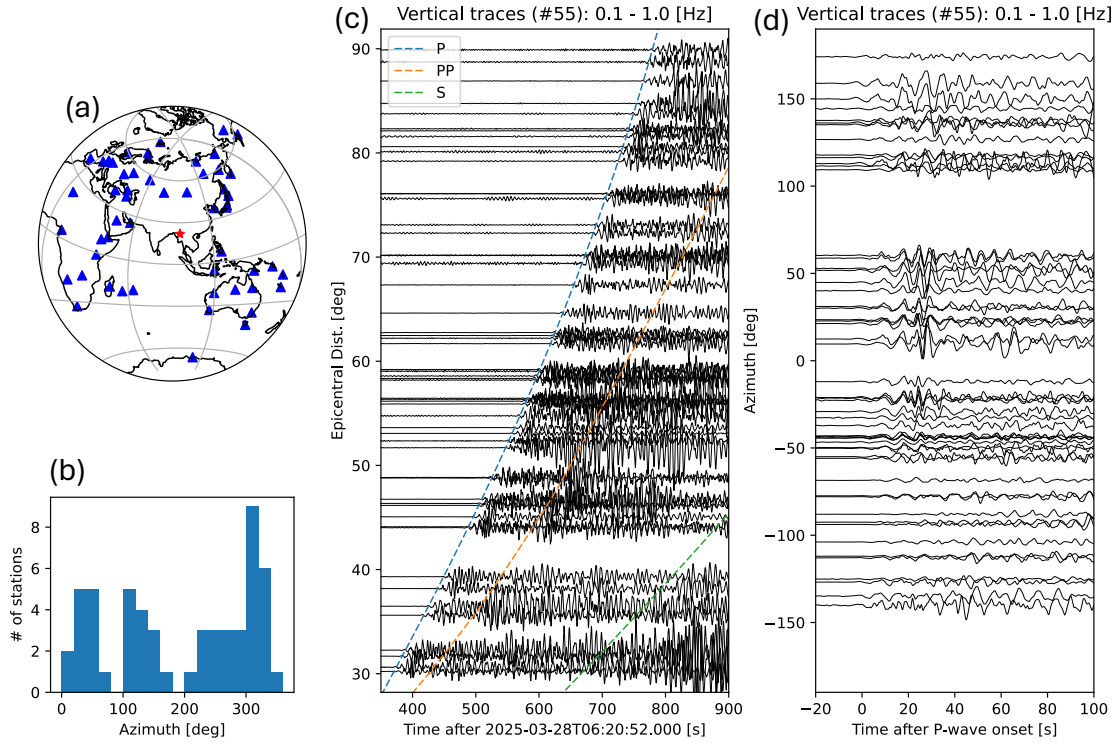

Figure S1: Same as Figure 2 in the main text, but for 0.1–1.0 Hz.

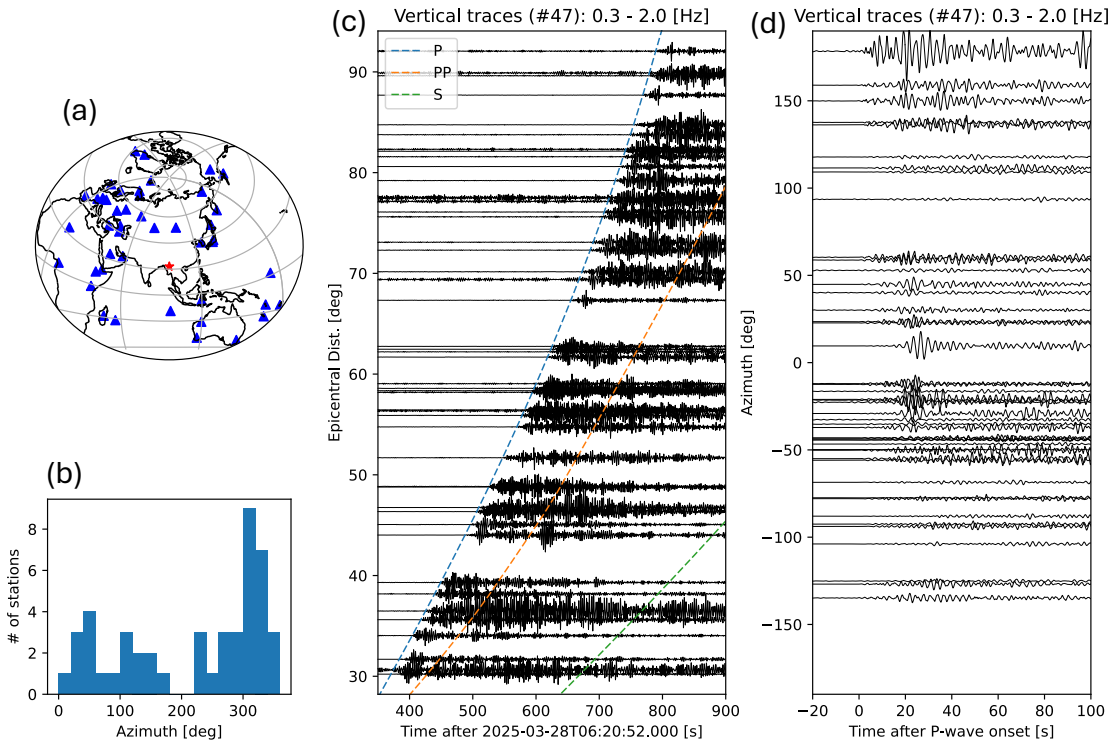

Figure S2: Same as Figure 2 in the main text, but for 0.3–2.0 Hz.

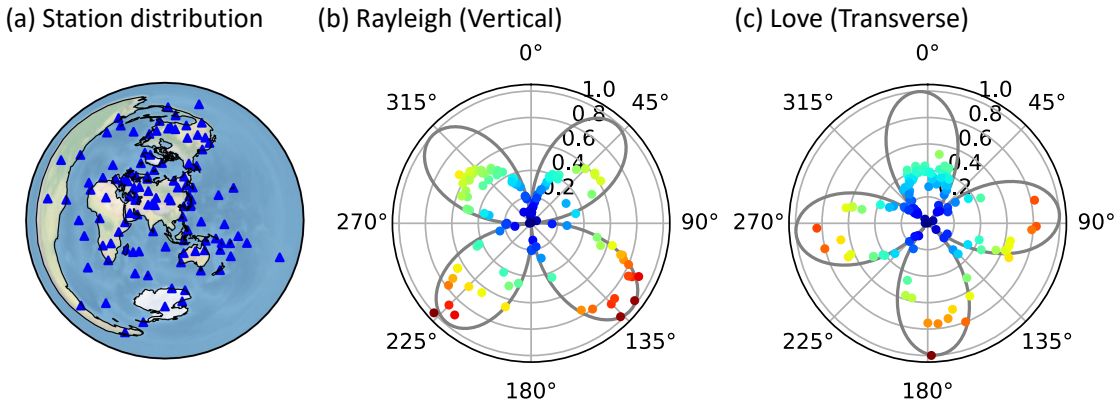

Figure S3: Surface-wave radiation patterns. (a) Map of stations used for amplitude measurements. (b) Azimuthal variations of normalized Rayleigh-wave amplitudes between 3 and 5 mHz. Colored dots show the normalized observed amplitude, where warm colors indicate larger amplitudes. The gray curve represents the theoretical point-source radiation pattern computed from the GCMT solution (blue beachball in Figure 1). (c) Same as (b), but for Love waves.

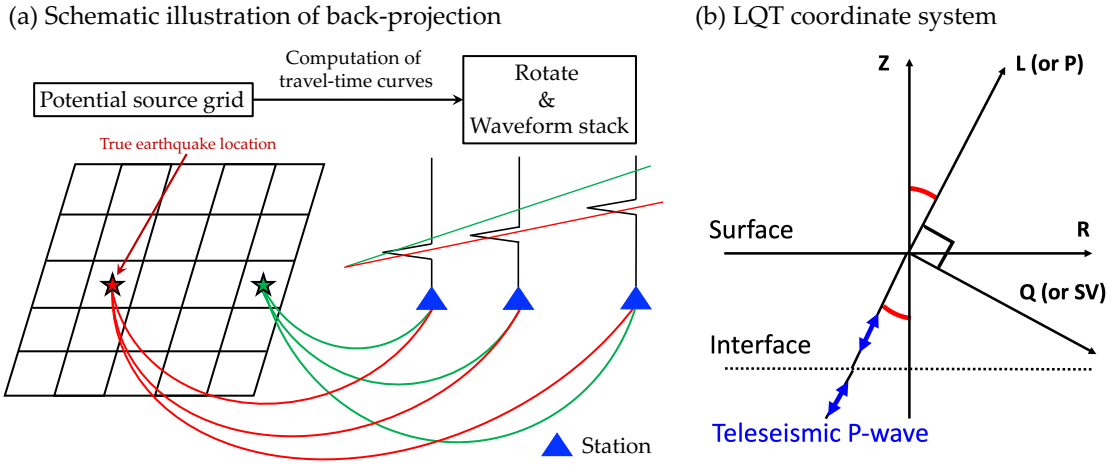

Figure S4: (a) Schematic illustration of the back-projection method. (b) Definition of the LQT coordinate system.

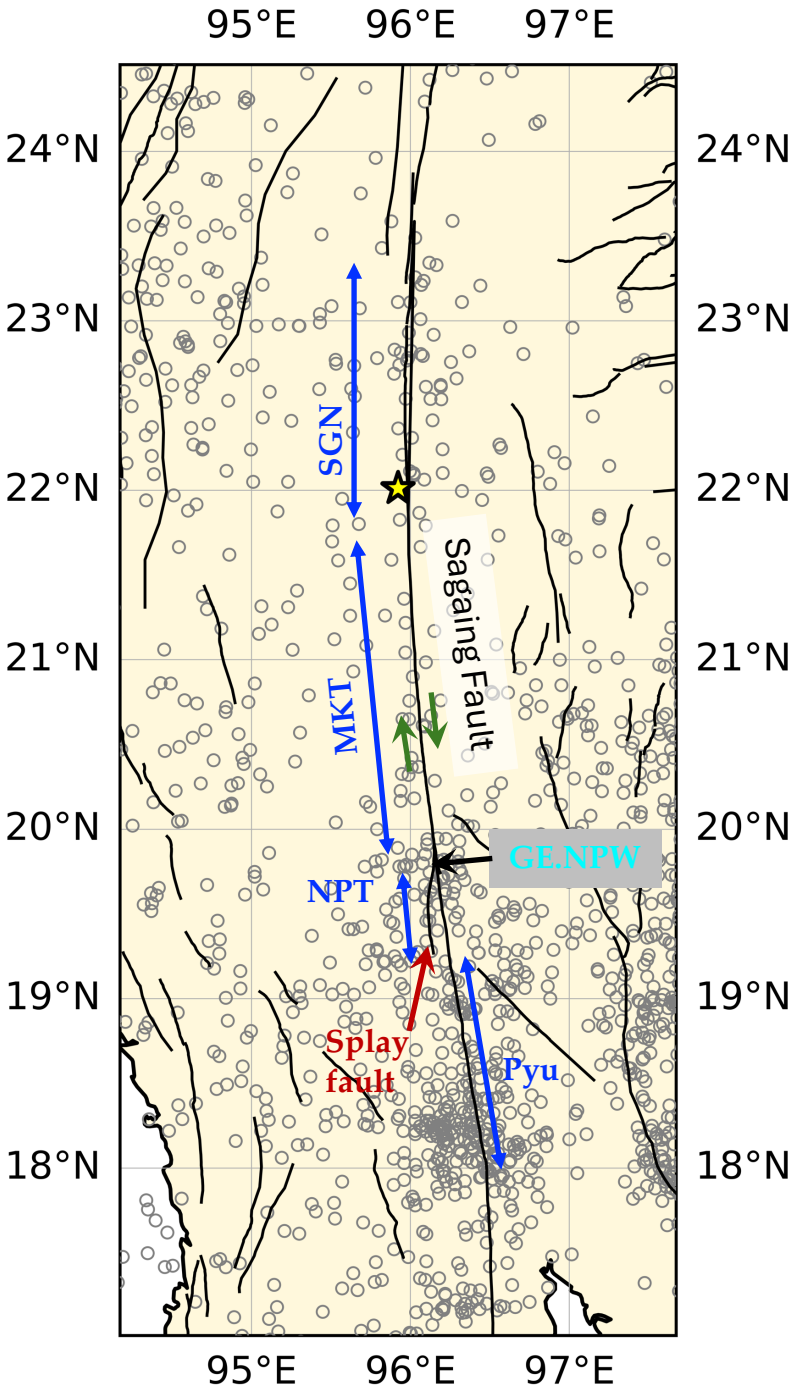

Figure S5: Background seismicity from the Thailand Meteorological Department (TMD). Symbols are the same as in Figure 1, except that gray circles indicate earthquakes occurring between 2012 and 27 March 2025.

Text S1: Baseline correction for time integration of acceleration waveforms at GE.NPW.

Following Watanabe et al. (2021), we assumed that coseismic slip generated step-like baseline shifts in the acceleration records. In this study, when performing time integration of the near-field acceleration records at GE.NPW, we applied baseline correction using the following piecewise equation (Equation 2 in Watanabe et al. (2021)):

$$a_{cor}(t) = \begin{cases} a(t) & (0 \le t \le t_1) \\ a(t) - \mathrm{C}_1 & (t_1 \le t \le t_2) \\ a(t) - \mathrm{C}_2 & (t_2 \le t \le 140\ s) \end{cases}$$

where $a_{cor}(t)$ and $a(t)$ denote the acceleration records after and before baseline correction, respectively, $\mathrm{C_i}$ represents the correction constant, and t_i denotes the start time of the correction relative to 2025-03-28T06:20:52.000 (UTC). The correction parameters are summarized in Table S1.

Table S1: Correction parameters used in this study. The reference time for $\boldsymbol{t_i}$ is 2025-03-28T06:20:52.000 (UTC).

	t_1 [s]	t_2 [s]	$\mathrm{C_1}$ [cm/s^2]	$\mathrm{C_2}$ [cm/s^2]
EW	62.0	82.0	-0.01	0.042
NS			-0.1	0.055
UD			0.0002	0.0175

Watanabe, T., Komatsu, M., Takenaka, H., 2021. Estimation of displacement waveforms by baseline correction of near-fault acceleration records of the 2016 Kumamoto earthquake with median filter (in Japanese with English abstract). Okayama University Earth Science Report. https://doi.org/10.18926/esr/61959